China Welding 35 (2026) 100028

Contents lists available at ScienceDirect

China Welding

journal homepage: www.keaipublishing.com/en/journals/china-welding/

Fatigue and creep damage behavior of aerospace-grade austenitic stainless steel GTAW joints: An X-ray diffraction residual stress analysis-based study

Jian Li[a], Danqi Zhang[b,*], Haijing Zhou[a], Chen Shen[b,c]

[a] China Astronautics Standards Institute, Beijing 100071, China
[b] Shanghai Key Laboratory of Materials Laser Processing and Modification, School of Materials Science and Engineering, Shanghai Jiao Tong University, Shanghai 200240, China
[c] Shanghai Changxing Ocean Laboratory, Shanghai 201913, China

ARTICLE INFO

Keywords:
SUS321 stainless steel
Fatigue
Creep
Residual stress
Aerospace-grade metal

ABSTRACT

With the continuous advancement of aerospace technology, ensuring the reliability of aerospace engines after testing is critical. While various methods exist for assessing fatigue life, non-destructive prediction based on in-situ X-ray diffraction (XRD) residual stress analysis remains underexplored—particularly for low-cycle fatigue in welded joints. This study proposes a novel approach that uses in-situ XRD to monitor residual stress evolution under fatigue and creep loading in gas tungsten arc welding (GTAW) joints of aerospace-grade austenitic stainless steel SUS321. Through metallographic observation, scanning electron microscopy (SEM), electron backscatter diffraction (EBSD), and in-situ XRD measurements, we demonstrate a strong correlation between longitudinal residual stress at the weld center and fatigue life. Under fatigue loading at 60 % of the ultimate tensile strength (UTS), longitudinal residual stress transitions from tensile to compressive with increasing cycles, and fatigue fracture occurs once residual stress approaches base metal levels (~ 0 MPa). In contrast, under creep loading, no clear trend in Y-direction residual stress was observed, limiting its utility for creep life prediction. This work establishes a reliable, non-destructive framework for evaluating the service life of welded aerospace components, offering a new methodology beyond conventional practices.

1. Introduction

Austenitic-based materials serve as essential high-temperature structural materials in various fields, including aviation, aerospace, marine engineering, energy, and chemical engineering. Among these materials, SUS321 is extensively employed in key components like combustion chambers and guide vanes of aero engines, as well as reaction kettles of aerospace hydrogen-oxygen engines. This is due to its ability to maintain relatively high tensile strength, fatigue resistance, creep resistance, and thermal corrosion resistance at elevated temperatures [1]. Welding serves as the primary processing and manufacturing method for aerospace structural components. However, the material properties of metallic alloys can undergo significant alterations under welding conditions, particularly their dynamic mechanical properties, which experience substantial changes. In structural components, the dynamic fatigue life of the welded joint often dictates the overall service life of the component.

Engine test runs are an indispensable step prior to the launch of a spacecraft. During these tests, the engine components endure dynamic loads approaching the material's yield strength, as well as significant creep effects. Consequently, evaluating the life attenuation of welds under low-cycle fatigue with plastic strain amplitude during testing and the consumption of high-temperature creep life is critical for ensuring the successful execution of the spacecraft launch mission. Welds located within the engine are typically inaccessible for removal post-test, and the associated components are generally not replaced. Additionally, destructive testing of these components is not feasible. Therefore, there is an urgent need for an effective non-destructive assessment method to determine whether the welds remain capable of withstanding subsequent launch tasks following the test run.

The state of weld residual stress is directly associated with fatigue loading. Weld residual stress is a self-equilibrating stress that manifests as tensile stress in the weld zone, often reaching or even exceeding the material's yield strength [2], while exhibiting relatively low

Peer review under the responsibility of Editoral Board of China Welding.
* Corresponding author.
E-mail addresses: zdq-june@sjtu.edu.cn (D. Zhang), cshen486@sjtu.edu.cn (C. Shen).

https://doi.org/10.1016/j.cwe.2026.100028
Received 30 April 2025; Received in revised form 11 January 2026; Accepted 26 January 2026
Available online 6 February 2026

compressive stress in regions distant from the weld zone. This implies that in an unloaded welded structure, there exists localized tensile stress equivalent to the material's yield strength. It is widely accepted that residual compressive stress inhibits fatigue crack propagation, thereby enhancing material fatigue resistance and extending service life, whereas residual tensile stress promotes crack initiation, thus reducing the service life of the material [3]. Relevant studies have demonstrated that even a minor welding residual tensile stress (less than 10 % of the yield strength) can substantially reduce the material's fatigue life (by up to 25 %). Conversely, residual compressive stress not exceeding 10 % of the yield strength can enhance the material's fatigue life by as much as 75 % [4]. When investigating the relationship between fatigue life and residual stress, researchers often focus on high-cycle fatigue life during the elastic deformation stage [5,6], whereas fewer studies address the low-cycle fatigue life associated with plastic strain amplitude. Moreover, common fatigue specimens, such as plate and round bar specimens [7], may experience changes in residual stress distribution due to mechanical processing deformation. Thus, it is crucial to investigate how to characterize the relationship between low-cycle fatigue life in the plastic deformation stage and residual stress. The performance of the engine welded joint at high temperatures significantly impacts the launch safety of spacecraft. During test runs and subsequent service, the engine is exposed to high-temperature creep loads. Research indicates that residual stress undergoes stress relaxation under thermal loading conditions. Nevertheless, regarding the fracture behavior of welded joints, there is no consensus on the influence of residual stress due to its dependence on factors such as weld type, welding process, and external load form.

According to whether the component is damaged during residual stress testing, the methods for measuring residual stress can be categorized into destructive, semi-destructive, and non-destructive techniques. Destructive methods include the contour method and the deep hole method, among others. Semi-destructive approaches encompass the drilling method and the indentation strain method. Non-destructive techniques comprise X-ray diffraction, synchrotron radiation X-ray diffraction, neutron diffraction, ultrasonic methods, and others [8]. Each residual stress testing method possesses distinct advantages and disadvantages. Among these, the X-ray diffraction method, which is grounded in Bragg's law, stands out as a non-destructive technique characterized by mature theoretical foundations and high measurement accuracy [9]. This method demonstrates particular advantages in engineering applications for non-destructively evaluating surface residual stresses.

This paper utilizes the XRD diffraction technique to perform "fatigue-in-situ measurement of X-ray residual stress" and "creep-in-situ measurement of X-ray residual stress" experiments. A comprehensive series of tests clarifies the evolution of weld residual stress under fatigue loading and creep conditions, thus offering a robust theoretical basis and dependable data support for evaluating the fatigue life and creep life of welds using non-destructive XRD stress measurement results.

2. Experimental details

2.1. Materials

The base material is a 4-mm-thick SUS321 stainless steel plate, featuring a 35° bevel (70° included angle) with a 1-mm land. The butt joint includes a 1-mm gap. Welding is performed in two passes using gas tungsten arc welding (GTAW), with a 1.2-mm-diameter TG-S347 welding wire (AWS ERNiFeCr-2) as the filler material. The compositional details of both the base material and the welding consumable are presented in Table 1.

To ensure the complete filling of the weld seam and achieve optimal structural integrity, the welding process is designed with a backing weld, followed by a fill weld and a cap weld, totaling three passes. This design significantly enhances the structural integrity of the weld seam. Moreover, the welding wire consists of an intricately combined dual-material structure, which enhances the efficiency of weld deposition. During the welding process, gas protection is implemented via a dual-system approach: argon gas supplied externally by the welding torch at a flow rate of 10 L/min and internally through the butt welding fixture plate at 1.5 L/min. This arrangement ensures complete inert gas coverage on both the front and back sides of the weld seam. To minimize deformation, the butt plates are firmly clamped during welding, thereby preventing any potential distortion from affecting subsequent mechanical sample preparation. Prior to welding, the area within 20 mm around the weld seam is thoroughly cleaned with acetone to eliminate contaminants and avoid inclusions. The welding parameters are detailed in Table 2.

2.2. Material characterization and mechanical property test

2.2.1. Material characterization

The weld metallographic specimens were prepared using the wire-cutting method. Subsequently, they were ground flat, polished, and electrolytically etched with a 10 % oxalic acid solution by volume. The electrolytic etching was conducted at a voltage of 9 V for 60 s. Microstructural characterization was performed using an AXIO Imager A2m metallographic microscope. For further analysis, the microstructure of the stainless steel was examined using a scanning electron microscope (SEM, TESCAN VEGA) equipped with a secondary electron (SE) detector. Electron backscatter diffraction (EBSD) tissue characterization was carried out using a scanning electron microscope (TESCAN MIRA3) integrated with an EBSD information acquisition system. The experimental conditions included an acceleration voltage of 20 kV, an electron beam current of 5 nA, and a working distance of 18 mm. Scanning ranges and step lengths were adjusted according to

Table 1
Chemical compositions of welding base materials and filler materials for GH4169 (wt%).

Alloys	Ni	Cr	Mo	Nb	Ti	C	P	S	Si	Mn	Cu	Fe
SUS321	9–12	17–19	N/A	N/A	0.7	0.08	0.045	0.03	1	2	N/A	Bal.
TG-S347	10	19.3	0.07	0.6	N/A	0.05	0.02	0.01	0.4	2.1	0.07	Bal.

Table 2
Parameters of the GTAW manual welding process.

Argon flow rate (L/min)	Welding current(A)	Welding speed (mm/min)	Wire feeding speed (mm/min)	Arc length(mm)
10 (Torch) 1.5 (Backing)	90 (First) 100 (Second)	400	500	2.5–3.5

specific requirements. The EBSD data were analyzed and processed using AztecCrystal 2.0 software developed by OXFORD. Prior to EBSD information acquisition, the specimens underwent accelerated vibration polishing to ensure high-quality surface preparation.

2.2.2. Tensile tests at room and elevated temperatures

Based on the actual service conditions of the hydrogen-oxygen reactor in aeroengines, the fatigue loading requirement was established at 60 % of the ultimate tensile strength (UTS). To determine the fatigue and creep load, tensile tests were conducted on weld samples under both room temperature and elevated temperatures (750 ℃, 800 ℃, and 850 ℃). The testing procedure adhered to the standard GB/T 2651–2008. The sampling schematic is illustrated in Fig. 1. Tensile tests were performed at a strain rate of 1 mm/min, and three replicate samples were tested to ensure data repeatability and reliability.

2.2.3. High-frequency low-cycle fatigue test at room temperature

Although the service temperature of the test material is high, no phase transformation occurs within the operational temperature range, and the temperature has negligible effects on the material's physical properties. Consequently, the stress variation law obtained at room temperature can be considered equivalent to that obtained at high temperatures. Three fatigue samples were randomly selected from different positions of the weld for room-temperature high-frequency low-cycle fatigue testing. The sampling schematic is presented in Fig. 2. The fatigue testing was conducted using a CRIMS® GPS100 machine with a vibration frequency of 110 Hz. The loading mode was tension-tension fatigue with a stress ratio (R) of 0.1.

2.2.4. Creep test

Three creep samples from different positions along the weld seam were randomly selected for high-temperature creep testing. Given that the primary service temperature range of the component is 750 ℃ to 850 ℃, the test temperatures were set at 750 ℃, 800 ℃, and 850 ℃, respectively. The sampling locations for the creep tests are illustrated in Fig. 2(a), while the dimensions of the creep samples are detailed in Fig. 2(c). The high-temperature creep tests were conducted using the testing machine manufactured by China National Machinery Test & Inspection Co., Ltd., with the applied load set at 60 % of the material's high-temperature tensile strength. To ensure reliable testing, the samples were securely fastened to the machine to prevent interruptions caused by loosening during creep loading. Additionally, the alignment of the clamping system was verified prior to testing.

2.3. In-situ measurement of X-ray residual stress

According to GB/T 7704–2017, the residual stress distribution of fatigue specimens was analyzed using the X-ray non-destructive testing method. The XRD residual stress measurement equipment employed was a PROTO® fixed XRD residual stress measuring instrument. Prior to conducting the measurements, the weld area of the sample was electrolytically polished to eliminate surface stresses induced by sample preparation, thereby enhancing the accuracy of the data. The electrolytic polishing process was performed at a voltage of 10–15 V for approximately 1 min.

From the perspective of sample processing, stress release in the x direction is relatively significant due to less constraint, whereas in the y direction, higher residual stress is expected because of the retained substrate's constraint. Given that the specimen size in the x direction is

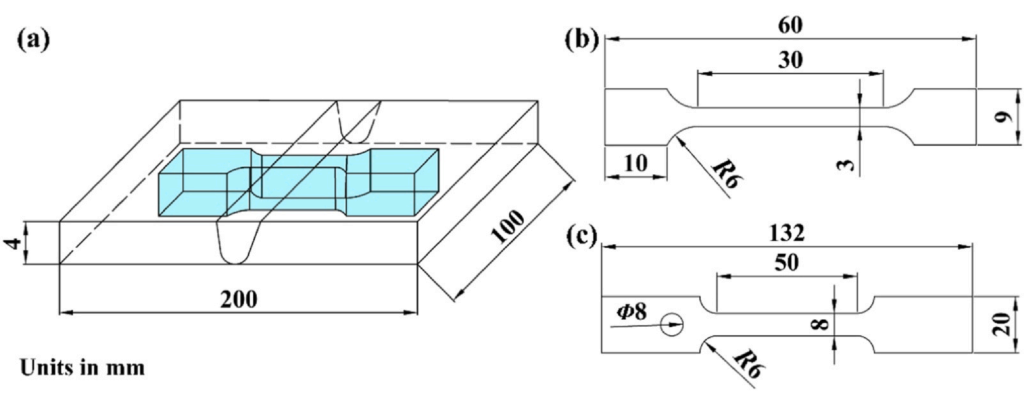

Fig. 1. Schematic and dimensions of tensile specimens at room and elevated temperatures:(a) Schematic diagram of the tensile specimen, (b) Dimensions of room-temperature tensile test specimens, (c) Dimensions of elevated-temperature tensile test specimens.

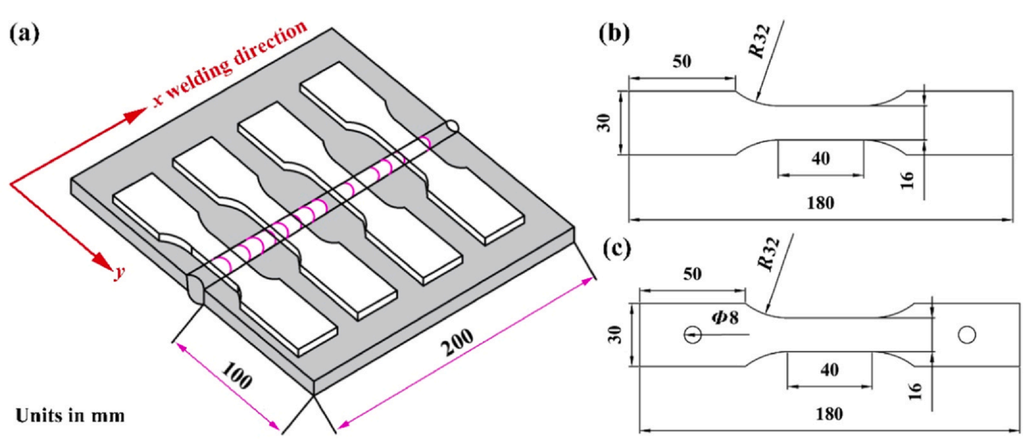

Fig. 2. Schematic of sampling and fatigue and creep specimens: (a) Schematic diagram of fatigue and creep specimens, (b) Dimensions of fatigue test specimens, (c) Dimensions of creep test specimens.

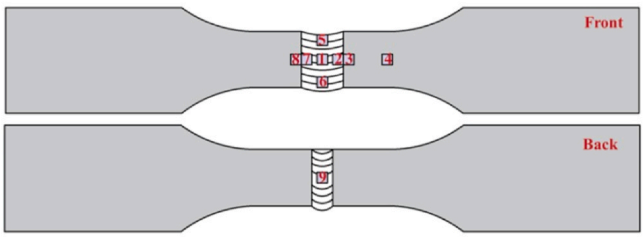

Fig. 3. Schematic diagram of sampling points for XRD residual stress measurement (units in mm).

smaller, it is more susceptible to cutting effects compared to the y direction. Consequently, greater attention is focused on the relationship between fatigue life and residual stress in the *y* direction of the weld. To explore the potential correlation between residual stress and fatigue life as comprehensively as possible, residual stress was measured at nine position points perpendicular to the weld in the plate plane (*y*), as illustrated in Fig. 3. Specifically, points 1, 5, and 6 are located at the weld centerline; points 2 and 7 are situated in the weld area 1 mm away from the fusion line; points 3 and 8 are positioned on the base metal side 1 mm away from the fusion line; point 4 is located within the base metal; and point 9 is at the center of the weld back. This arrangement of measurement points aims to validate the influence of measurement location on the results and provide data support for selecting subsequent measurement points through confirmatory tests. By applying a certain number of fatigue or creep cycles and supplementing with XRD residual stress measurements, the variation law of residual stress at each weld position under fatigue loading is determined.

2.4. Residual stress calculation method

For polycrystalline materials, the macroscopic stress-induced strain is regarded as the statistical average of lattice strains within the corresponding region. Consequently, residual stress can be determined by evaluating the lattice strain using the principles of X-ray diffraction. Based on the classification of residual stresses, the procedures for calculating two-dimensional planar residual stress and three-dimensional residual stress are outlined as follows [10]:

Under the plane stress state, $\tau_{B} = \tau_{22} = \sigma_{33} = 0$, it can be derived that:

$$\varepsilon_{\varphi\psi}^{hkl} = S_1^{hkl}(\sigma_{11} + \sigma_{22}) + \frac{1}{2}S_2^{hkl}(\sigma_\varphi + \sin^2\psi) \tag{1}$$

The differential of the square of $\sin^2\psi$ in Eq. (1) can be obtained as follows.

$$\sigma_\varphi = \frac{1}{(1/2)S_2^{hkl}}\frac{\partial\varepsilon_{\varphi\psi}^{hkl}}{\partial\sin^2\psi} \tag{2}$$

where $\varepsilon_{\varphi\psi}^{hkl}$ represents the normal strain in the (φ, ψ) direction; ψ is the angle between the strain vector $\varepsilon_{\varphi\psi}$ and the z-axis, and φ also denotes the angle between the projection of $\varepsilon_{\varphi\psi}$ onto the *xOy* plane and the *x*-axis; $S_1^{\{h,k,l\}}$ and $S_2^{\{h,k,l\}}$ are the *x*-ray elastic constants of the {*hkl*} crystal plane, which are related to the material's Young's modulus E and Poisson's ratio ν; $\sigma_\varphi$indicates the orientation of the stress to be measured.

When the three-dimensional stress is distributed, the functional relationship between $\varepsilon_{\varphi\psi}^{hkl}$ and $\sin^2\psi$ exhibits an elliptical curve. Based on the formula below, σ_φ and τ_φ can be determined using the least squares method.

$$\varepsilon_{\varphi\psi}^{hkl} = S_1^{hkl}(\sigma_{11} + \sigma_{22}) + \frac{1}{2}S_2^{hkl}(\sigma_\varphi + \sin^2\psi) + \frac{1}{2}S_2^{hkl}(\tau_\varphi + \sin 2\psi) \tag{3}$$

Under three or more distinct φ values, several $\pm\psi$ angles are respectively designated for measurement, enabling the calculation of the stress tensor.

When preferred orientation exists in the material, both $\varepsilon_{\varphi\psi}^{\{hkl\}}$ and $\sin^2\psi$ exhibit a significant oscillatory distribution. The peak shape remains largely unchanged, while the diffraction peaks show a gradual broadening trend. For different ψ angles, the variation in peak intensity is substantial, and the choice of radiation and crystal planes significantly influences the accuracy of residual stress X-ray test results. A higher multiplicity factor of the crystal plane reduces the impact of texture on the accuracy of the test results. The non-random grain orientation in anisotropic materials has a pronounced effect on the shape or relative intensity of the peaks. If the sampled area contains large grains, such as well-developed dendrites or coarse-grained welds, and the stress level is high, the limited number of grains participating in diffraction leads to low peak intensity and poor accuracy of the peak position at various ψ angles. Since X-ray residual stress testing is based on elastic theory and assumes that the material is homogeneous, continuous, and isotropic, real materials often deviate from these assumptions due to their inherent anisotropy. Consequently, the relative change in crystal plane spacing is measured only on some surface grains. In conclusion, the accuracy of X-ray residual stress test results is significantly influenced by factors such as the test site, grain size, and degree of preferred orientation.

3. Results and discussion

3.1. Microstructure

To avoid the influence of the non-uniform and unstable microstructure of the welded joint on the fatigue and creep test results, a detailed study and analysis of the microstructure of the welded joint were conducted. Visual inspection of the welded joint reveals no cracks, collapses, burn-throughs, or other defects in the weld. The metallographic microstructure of the base metal for austenitic stainless steel SUS321 is presented in Fig. 4(a). At room temperature, the microstructure exhibits a single-phase austenite structure with twins. After solution treatment, SUS321 austenitic stainless steel demonstrates low hardness, excellent toughness, high plasticity, and superior corrosion resistance. The microstructure of the SUS321 austenitic stainless steel welded joint is illustrated in Fig. 4(b-c). The weld and the base metal are well bonded. In the heat-affected zone (HAZ), the grains exhibit a tendency to grow; however, this growth is not pronounced. The weld zone displays a typical columnar crystal structure.

Inverse pole figure (IPF) and Kernel Average Misorientation (KAM) diagrams of the SUS321 stainless steel welded joint are presented in Fig. 5. In the IPF map (Fig. 5(a)), regions with different colors correspond to grains and sub-grains with distinct crystallographic orientations. Adjacent to the fusion line (marked as a pink dotted line in Fig. 5(a)), the weld microstructure comprises coarse columnar grains that predominantly grow along the $< 100 >$ direction and are oriented approximately perpendicular to the fusion line. The heat-affected zone (HAZ) and base metal display typical massive austenite structures with isotropic grain orientation, exhibiting no preferred orientation due to the influence of the welding thermal cycle. Stress concentration within the HAZ and weld primarily occurs at grain boundaries, particularly on the side adjacent to the fusion line. During welding, high temperatures and thermal stresses in the HAZ promote dislocation movement. Consequently, dislocations of the same type on the same slip plane glide and accumulate at the grain boundaries, forming dislocation walls. With continuous accumulation and entanglement, these dislocations progressively develop into cellular block structures and eventually evolve into substructures.

Fig. 5(b) presents the local orientation difference distribution map near the fusion line of the welded joint, also referred to as the KAM map. The local orientation difference serves as an indicator for measuring the degree of grain deformation and dislocation density. It is calculated based on a core point consisting of 24 nearest neighboring points, where each core point (100 nm × 100 nm) is assigned a scalar value representing its local orientation difference. The KAM value can

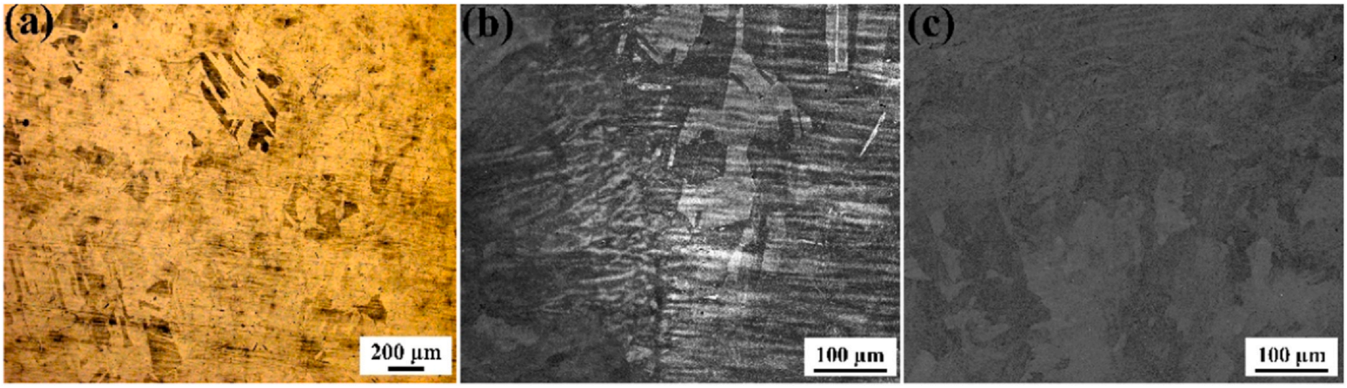

Fig. 4. Microstructures of SUS321 stainless steel welded joint in different regions: (a) OM microstructure of base metal, (b) SEM microstructure near the fusion line, (c) SEM microstructure in the weld.

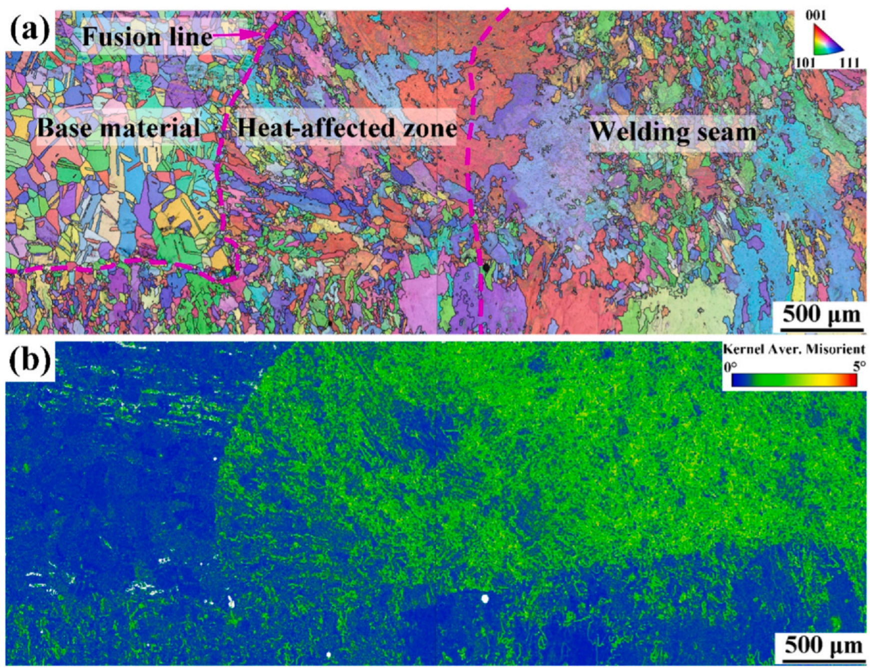

Fig. 5. EBSD analysis results near the fusion line: (a) IPF, (b) KAM.

be determined using the following formula [11]

$$KAM = \exp[\frac{1}{N}\sum_{1}^{i} \ln KAM_{L,i} \tag{4}$$

Where $KAM_{L,i}$ is the local KAM value at point i, and N is the number of points in the test area.

The geometric dislocation density can be calculated by the following formula [12]

$$\rho^{GND} = \frac{2\Delta\theta_i}{ub} \tag{5}$$

Where $\Delta\theta_i$ is the average value of the local orientation difference of the selected area, μ is the step size, and b is the Burgers vector.

It is evident that significant residual strains exist in the weld seam and HAZ. By integrating the information from the IPF mapping and KAM diagram, it can be observed that stress concentration in the HAZ and weld seam predominantly occurs at the grain boundaries, particularly in the HAZ adjacent to the fusion line. Macroscopically, this manifests as a relatively high level of residual stress in the weld seam and the HAZ near the fusion line.

3.2. Tensile property

The stress-strain curves of SUS321 austenitic stainless steel at both room temperature and high temperature are presented in Fig. 6. Dynamic recrystallization [13] was observed during the tensile deformation process of SUS321 austenitic stainless steel. As a result, the stress-strain curve exhibited a wavy pattern due to the alternating effects of dynamic recrystallization and work hardening. For the room temperature tensile tests, the UTS of the three samples were measured as 664 MPa, 680 MPa, and 718 MPa, respectively, yielding an average UTS value of 687.3 MPa. By calculating the cross-sectional area to be 40 mm^2, the load corresponding to 60 % of the UTS was determined to be 16.5 kN. The stress-strain curves obtained at 750 °C, 800 °C, and 850 °C are presented in Fig. 6(b). The ultimate tensile strength (UTS) values were measured as 156 MPa at 750 °C, 108 MPa at 800 °C, and

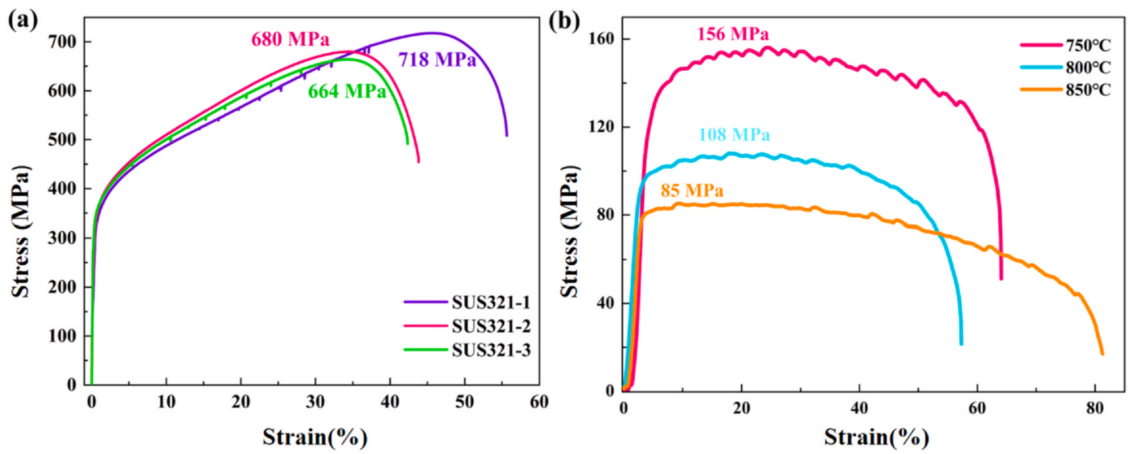

Fig. 6. Engineering stress-strain curves of SUS321 stainless steel GTAW welds: (a) At room temperature, (b) At elevated temperatures.

85 MPa at 850 ˚C. Upon calculating the cross-sectional area to be 40 mm^2, the corresponding 60 % UTS loads were determined to be 6.24 kN at 750 ˚C, 4.32 kN at 800 ˚C, and 3.4 kN at 850 ˚C. The fracture position of the tensile specimen is located near the fusion line. Based on the aforementioned analysis of the microstructure of the welded joint, the weld microstructure near the fusion line consists of interlaced columnar crystals. The boundaries of these columnar crystals are regions where impurities, shrinkage cavities, and pores tend to accumulate, making them weak points in terms of mechanical performance. Additionally, stress concentration in the heat-affected zone (HAZ) near the fusion line is pronounced, ultimately resulting in the tensile specimen fracturing at this location.

3.3. Analysis of in-situ fatigue- X-ray residual stress

Fig. 7 shows the calculation results of residual stress variation with fatigue cycle numbers for three parallel samples. It can be seen from Fig. 7 that the base metal position (point 4) has a stable microstructure. The residual stress remains essentially unchanged with increasing fatigue cycles and stays below 50 MPa. Points 2 and 8, located near the fusion line on the base metal side, experience a welding thermal cycle process, which acts like stress-relief annealing and results in a stress state similar to that of the base metal. As a result, their residual stress states are largely unaffected by the number of fatigue cycles. In contrast, the residual stress at point 9 shows no clear trend. Since it is located on the back of the weld, where the microstructure is unstable, point 9 is not suitable as an X-ray residual stress measurement point for evaluating fatigue life.

The residual stress states at points 2 and 7, located in the weld area near the fusion line, gradually align with the stress state of the base metal. However, the XRD residual stress test results for these points are significantly influenced by columnar crystal structures and microstructural texture. Points 1, 5, and 7 are all situated on the weld centerline, corresponding to the highest point of the weld reinforcement, and exhibit similar trends: they transition from tensile stress states toward a stress level approaching 0 MPa. Nevertheless, points 5 and 7, being positioned at the sample edges, are substantially affected by residual stress release during sample preparation, leading to less pronounced changes in residual stress levels compared to point 1. Additionally, the XRD residual stress test result for point 1 is less susceptible to interference from columnar crystals and microstructural texture.

With the increase in fatigue cycle times, dislocations are activated, and residual stress is gradually released. This phenomenon is primarily attributed to the presence of a large number of twin boundaries in the matrix, which reduces the total interfacial energy of the system. Dislocations can glide on twin planes. Moreover, dislocations bypass precipitated phases, maintaining the number of mobile dislocations, while dislocation reorganization simplifies the dislocation configuration. When the load reaches 60 % of the UTS, it exceeds the yield strength of SUS321 stainless steel, causing cyclic strain to enter the plastic deformation range. Cyclic plastic deformation occurs in regions with localized stress or stress concentrations. As cyclic loading continues, cracks initiate in the weaker regions of these localized plastic zones and subsequently propagate within the plastic area, gradually evolving into macroscopically detectable cracks. Under cyclic stress, cracks further traverse through the plastic region, continuing to grow until final fracture.

When the stress reaches equilibrium throughout the workpiece or within a large macroscopic region, it is referred to as macroscopic stress

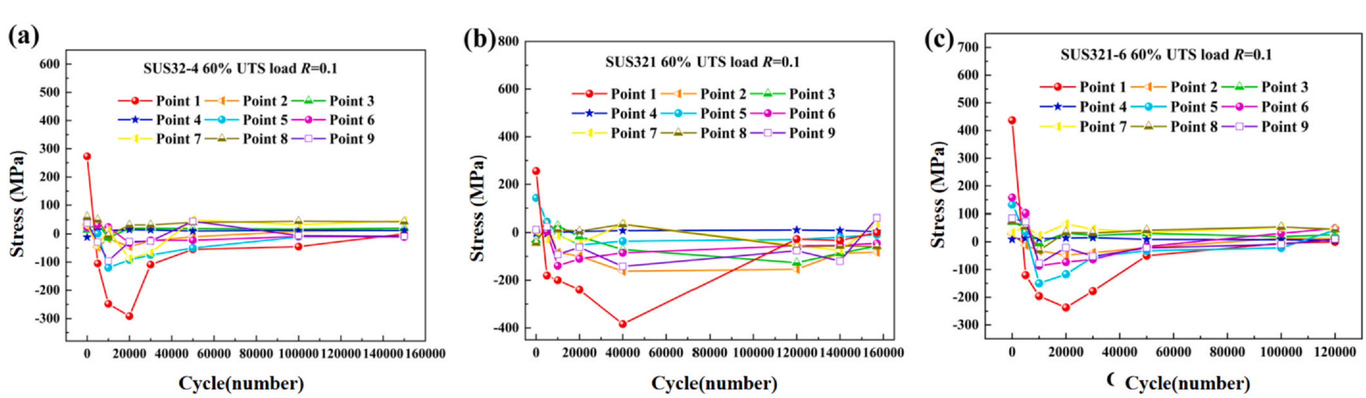

Fig. 7. The calculation results for residual stress variation with fatigue cycle numbers for three parallel samples, respectively: (a) SUS321–1, (b) SUS321–2, (c) SUS321–3.

or the first type of stress. Fundamentally, the presence of welding residual stress can primarily be attributed to the extremely high temperatures during welding and the rapid cooling that follows. This substantial temperature variation inevitably induces thermal expansion and contraction effects. his represents the fundamental reason for the presence of welding residual stress. Additionally, during the welding process, temperature variations occur across different regions of the material, which also constitutes a critical factor contributing to the significant level of welding residual stress. The residual stress perpendicular to the weld direction results from the combination of residual stress induced by longitudinal shrinkage in the plastic deformation zone near and within the weld, as well as the residual stress caused by non-simultaneous transverse shrinkage in the same plastic deformation zone. During the welding process, the welding zone is rapidly heated at a significantly higher rate compared to the surrounding areas, causing partial melting. The materials in the welding zone expand thermally, but this expansion is constrained by the cooler adjacent regions, leading to the development of elastic thermal stress. As the temperature in the heated area increases, the yield strength decreases, allowing the thermal stress to partially exceed the yield limit. Consequently, plastic thermal compression is induced in the welding zone. Upon cooling, this region becomes relatively contracted, narrowed, or reduced in comparison to the surrounding areas, resulting in tensile residual stress within this zone. As illustrated in Fig. 7, the residual stress in the weld zone of the specimen without fatigue cyclic loading (i.e., 0 fatigue cycles) manifests as residual tensile stress. Based on the research findings of Masubuchi and Martin [14], the distribution of longitudinal residual stress σ_x can be calculated using the following formula:

$$\sigma_x(y) = \sigma_{\mathrm{m}}\left[1-\left(\frac{y}{b}\right)^2\right]\exp\left[-\frac{1}{2}\left(\frac{y}{b}\right)^2\right] \tag{6}$$

Where, σ_{m} is the maximum residual stress, and b is the width of the longitudinal residual stress zone.

It can be derived from the formula that the residual stress value at the weld center is the highest. In conjunction with the project's test results, it is evident that the residual stress at point 1 in the weld center position exhibits the most significant variation under the application of fatigue loads. Furthermore, the geometric dimensions of the weld seam play a crucial role in influencing the fatigue strength of the welded structure. Ninh et al. [15] experimentally demonstrated that increasing the transition angle can effectively enhance the fatigue strength. Taiwanese scholars [16] argue that increasing the transition angle yields a more significant improvement compared to enhancing the transition radius. However, research findings in the literature indicate that the weld transition radius also plays a crucial role in the fatigue strength of the joint. Specifically, when the transition radius is increased while keeping the transition angle constant, the fatigue strength of the joint improves. Johan [17,18] performed a fatigue life assessment of the butt joint with reinforcement, and scholars from MIT [18] also investigated the influence of the reinforcement. They unanimously concluded that removing the reinforcement enhances fatigue strength. Notably, point 1 at the weld center corresponds to the location with the largest reinforcement size. In summary, greater attention should be directed toward the variation in residual stress levels at the weld center (i.e., the position with the largest reinforcement size) as the number of fatigue cycles increases. As shown in Fig. 7, under a dynamic fatigue load of 60 % UTS, during the early stage of fatigue loading ($<$ 50,000 cycles), the residual stress level exhibits a pronounced downward trend. Xie et al. [19] conducted experimental research demonstrating that the release of welding residual stress is influenced by factors such as the initial residual stress distribution, yield stress, fatigue load amplitude, and the number of cycles. Dehkordi et al. [20] experimentally confirmed that the majority of welding residual stress release occurs during the first few load cycles. In general, the release of welding residual stress is also affected by the magnitude, direction, and duration of static loads, as well as the material properties of the structure. This phenomenon can be attributed to the activation of dislocations with increasing fatigue cycle times, leading to the gradual release of residual stress. Specifically, the presence of a large number of twin boundaries in the matrix reduces the total interfacial energy of the system, allowing dislocations to slip on twin planes. Additionally, dislocations bypass precipitated phases, maintaining a sufficient number of mobile dislocations, while dislocation reconstruction simplifies the dislocation configuration. These factors collectively contribute to the release of residual stress and the reduction of residual stress levels under dynamic fatigue loading. Furthermore, when the residual stress value at point 1 approaches that of the base metal (approximately 0 MPa), fatigue fracture is initiated. It can be observed from Fig. 7 that as the number of fatigue cycles increases, the tensile stress at point 1 of the fatigue specimen gradually decreases and transforms into a lower stress level before eventually releasing completely. Specifically, the residual stress at point 1 transitions from tensile stress to low stress and then gradually dissipates. When the residual stress at point 1 reaches a value equivalent to that of the base metal (approximately 0 MPa), fatigue fracture occurs. This phenomenon is attributed to the fact that the 60 % UTS fatigue load applied to the SUS321 specimen exceeds its yield strength, thereby causing cyclic strain to enter the plastic deformation range. Consequently, cyclic plastic deformation occurs in localized stress or stress concentration areas. As cyclic loading continues, cracks initiate in the weaker regions of these localized plastic zones and subsequently propagate within the plastic zone, gradually growing into macroscopic cracks detectable by conventional means. Under the influence of cyclic stress, these cracks further penetrate through the plastic zone and continue to propagate until final fracture occurs. Overload treatment can effectively reduce the residual stress in structures. The primary mechanism involves the superposition of the non-uniform welding residual stress field with the stress field induced by an externally applied load. This superposition causes certain regions with higher residual stresses to reach the material's yield stress, leading to localized plastic deformation. As loading continues, the region undergoing plastic deformation gradually expands. After unloading following a sustained period of overload, the residual stress is significantly diminished. The extent of welding residual stress reduction through overload treatment depends on the magnitude of the applied overload. The residual stress remaining after overload treatment can be expressed as σ_γ [21]:

$$\sigma_\gamma = \sigma_{\mathrm{s}} - \sigma_{\mathrm{ov}} \tag{7}$$

Where σ_{s} is yield strength; σ_{ov} is stress produced by overload.

When the stress induced by the external load on the welded part is superimposed with residual stress and exceeds the yield limit, plastic deformation occurs in a localized area of the welded part. If the external load is removed at this point, the component cannot return to its original geometric shape and the distribution of residual stress is altered. Consequently, during the 60 % UTS fatigue loading - in-situ X-ray residual stress test of the SUS321 specimen, after a certain number of cycles under dynamic fatigue loading exceeding the yield strength, the load is unloaded. This results in changes to the external load acting on the weld and redistribution of stress. During the application of external loading, the specimen experiences tensile stress. After unloading, to prevent deformation of the specimen, the residual stress transforms into compressive stress.

To summarize, for SUS321 specimens subjected to fatigue loads exceeding the yield strength (e.g., 60 % of the UTS), the longitudinal residual stress at the weld center gradually decreases with increasing fatigue cycles. Notably, within the first 50 000 cycles, the residual stress level exhibits a significant drop. Furthermore, the stress transitions from tensile to compressive. Ultimately, when the residual stress aligns with that of the base metal (approximately 0 MPa), fatigue fracture ensues. In conclusion, as long as residual stress remains present, the specimens retain fatigue life, which is independent of the material properties of the tested samples.

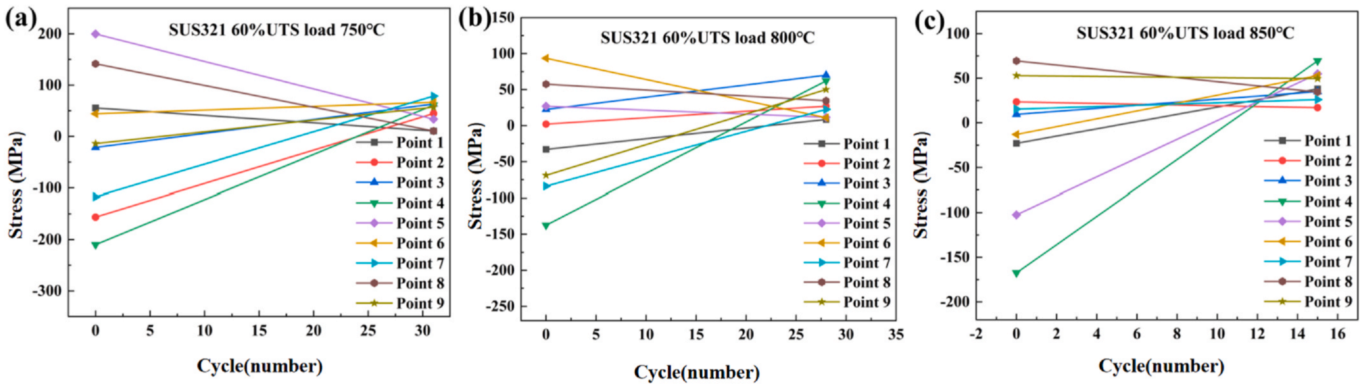

Fig. 8. The residual stress in the *y* direction of SUS321 changes with creep loading at different temperatures: (a) 750 °C, (b) 800 °C, (c) 850 °C.

3.4. Analysis of in-situ creep- X-ray residual stress

This section investigates the potential of using the XRD residual stress method for predicting high-temperature creep life, paralleling our approach for fatigue. The evolution of residual stress in the Y-direction for three SUS321 specimens under creep loading at 750 ℃, 800 °C, and 850 °C is presented in Fig. 8(a-c). A consistent trend is observed across all temperatures: after the application of a 60 % UTS creep load, the residual stress in the weld area rapidly relaxes to a low-stress state (0–50 MPa). This relaxation occurs early in the creep life and remains stable until fracture, with no systematic variation that correlates with the remaining creep life (31 h at 750 °C, 28 h at 800 °C, and 15 h at 850 °C).

The creep deformation mechanism of austenitic stainless steel at high temperatures is governed by dislocation motion [22]. Hence, for the X direction, we can expect the residual stress evolution under creep loading to be consistent with that in the *y* direction, based on the structural constraint characteristics and the high-temperature creep mechanism of SUS32. This consistency is attributed to the fact that high-temperature creep of SUS321 is dominated by dislocation self-diffusion and climb, a mechanism with no directional dependence. Thus, the stress relaxation effect acts uniformly in both the *x* and *y* directions, leading to consistent evolutionary trends. Below the yield stress, the primary mechanisms involve dislocation self-diffusion and climb, which are associated with relatively low creep activation energy. The pre-existing dislocation structure facilitates multi-directional slip during creep, effectively releasing stress, preventing stress concentration, and ultimately delaying the initiation and propagation of cracks. At temperatures of 750 ℃, 800 ℃, and 850 ℃, three SUS321 specimens were subjected to a creep load equivalent to 60 % of the UTS. The XRD residual stresses at each test point were fully relaxed to the range of 0–50 MPa. This is primarily attributed to the fact that the 60 % UTS creep load for the SUS321 alloy at high temperatures is lower than its yield strength, leading to creep deformation mechanisms dominated by dislocation activity. Below the yield stress, the primary processes involve self-diffusion and climb of dislocations, which effectively contribute to stress relaxation. To summarize, under a 60 % UTS creep load at various high temperatures, the change trend of residual stress in the Y direction within the weld area remains consistent. Consequently, it is challenging to assess the creep life state through non-destructive evaluation of residual stress in the weld zone. Nevertheless, given that the high-temperature creep life of SUS321 austenitic stainless steel significantly exceeds its service life, attention should be directed toward investigating the variation pattern of residual stress in the weld area under fatigue loading conditions. When the residual stress value at point 1 approaches that of the base metal (approximately 0 MPa), fatigue fracture is initiated. As the core focus of this study is to establish the non-destructive evaluation method based on residual stress, the detailed fatigue fracture mechanism is not elaborated in depth. However, combined with the existing microstructural and residual stress evolution data, the fatigue fracture process can be reasonably inferred: The crack initiates at the weld center (point 1), where the initial residual tensile stress is the highest and weld reinforcement is the largest. Cyclic plastic deformation activates dislocation slip along twin planes, leading to microcrack initiation at columnar crystal interfaces and high-dislocation-density regions. During propagation, the stable release of residual stress (tensile → compressive → ~0 MPa) regulates crack growth, resulting in fatigue striations on the fracture surface. This inferred fracture behavior further supports the correlation between weld center residual stress and fatigue life. Similar to the fatigue analysis, the detailed creep fracture mechanism is not the research focus of this work; instead, we emphasize the residual stress evolution law under creep loading. Notably, the residual stress has been fully relaxed to 0–50 MPa in the early creep stage (Fig. 8), so creep fracture is dominated by microstructure evolution rather than residual stress, which explains the non-correlation between residual stress and creep life.

4. Conclusions

Aerospace engine structural components typically must endure the combined effects of centrifugal force, vibration stress, rapid temperature fluctuations, and gas corrosion, among others, making them highly susceptible to low-cycle fatigue failure. To effectively assess whether an aerospace engine after a test run is capable of fulfilling subsequent spacecraft launch missions, a fatigue life prediction method based on X-ray diffraction is proposed. Through the in-situ measurement test of fatigue-induced X-ray residual stress, the following conclusions are drawn:

(1) The feasibility of assessing the fatigue life state through non-destructive residual stress measurement in fusion weld seams has been demonstrated. The longitudinal residual stress at the weld center exhibits a strong correlation with the fatigue life of the welded component. This location experiences the most significant changes in residual stress under fatigue loading, and XRD stress measurements at this point are less influenced by columnar crystals and microstructural texture, making it an appropriate measurement point for evaluating fatigue life.
(2) The longitudinal residual stress at the weld center exhibits a strong correlation with the fatigue life of the welded component. Under a fatigue load of 60 % UTS, as the number of fatigue cycles increases, the longitudinal residual stress at the weld center transitions from tensile to compressive. Fatigue fracture occurs when the residual stress value reaches equilibrium with that of the base metal, corresponding to a stress level of 0 MPa.
(3) When the fusion welding seam is subjected to high-temperature creep loading, the XRD residual stress at each test point is relieved to

approximately 0 MPa. The change trend of residual stress in the y direction within the weld zone exhibits no significant difference, making it challenging to predict the creep life based solely on the variation trend of the residual stress level in the fusion welding seam.

CRediT authorship contribution statement

Jian Li: Writing – original draft, Writing – review and editing, Data curation, Investigation, Funding acquisition. **Chen Shen**: conceptualization, supervision. **Haijing Zhou**: Methodology, curation, Formal analysis, Resources, supervision. **Danqi Zhang**: Reviewing and editing.

Funding

This work was financially supported by the Fundamental Research Funds for the Central Universities, the Institute of Marine Equipment, the Shanghai Rising-Star Program of Science and Technology Commission of Shanghai Municipality (Grant No. 23QA1404700), National Natural Science Foundation of China (Grant Nos. 52475384, 52505409), and China Postdoctoral Science Foundation (Grant No. 2024M761963).

Declaration of Competing Interest

The authors declare that they have no known competing financial interests or personal relationships that could have appeared to influence the work reported in this paper.

Acknowledgement

The authors gratefully acknowledge financial support from the Fundamental Research Funds for the Central Universities and Institute of Marine Equipment, Shanghai Rising-Star Program of Science and Technology Commission of Shanghai Municipality (Grant No. 23QA1404700), National Natural Science Foundation of China (Grant No. 52475384, 52505409), and China Postdoctoral Science Foundation (Grant No. 2024M761963).

References

[1] Li Y, Wang C. The role of austenite grain size on martensite start temperature and phase transformation path in SUS321 stainless steel. Mater Lett 2023;342:134313. https://doi.org/10.1016/j.matlet.2023.134313.

[2] Théodore J, Girault B, Couturier L, et al. Investigation of the residual stresses and strains, microstructure and mechanical properties of stainless steel multipass welds produced using dual wire-tungsten inert gas process. Materialia 2025;40:102403. https://doi.org/10.1016/j.mtla.2025.102403.

[3] Becker N, Kuhn D, Piochowiak J, et al. Fatigue life enhancement via residual stress engineering due to local forming during refill friction stir spot welding. J Mater Res Technol 2025;36:2951–9. https://doi.org/10.1016/j.jmrt.2025.03.205.

[4] Hendrato, Azka M, Muslih MR, et al. Fatigue crack growth and residual stress in simultaneous double-sided friction stir welded aluminum alloy AA6061-T6. J Adv Join Process 2025;11:100300. https://doi.org/10.1016/j.jajp.2025.100300.

[5] Herbert C, Axinte DA, Hardy M, et al. Influence of surface anomalies following hole making operations on the fatigue performance for a nickel-based superalloy. J Manuf Sci Eng 2014;136(5):051016. https://doi.org/10.1115/1.4027619.

[6] Chen Z, Moverare J, Peng RL, et al. Surface integrity and fatigue performance of Inconel 718 in wire electrical discharge machining. 3rd CIRP Conf Surf Integr (CIRP CSI) 2016;45:307–10. https://doi.org/10.1016/j.procir.2016.02.053.

[7] Rodríguez J, Aldabagh S, Alam MS. Low-cycle fatigue performance of ASTM A955 grade 520 and CSA G30.18 400W reinforcing bars including the effect of inelastic buckling. Constr Build Mater 2025;476:141005. https://doi.org/10.1016/j.conbuildmat.2025.141005.

[8] Viotti MR, Kaufmann GH. Accuracy and sensitivity of a hole drilling and digital speckle pattern interferometry combined technique to measure residual stresses. Opt Lasers Eng 2004;41(2):297–305. https://doi.org/10.1016/S0143-8166(02)00173-2.

[9] Pan B, Ma L, Xia Y. A novel technique for measuring 3D deformation of adhesively bonded single lap joint. Sci China Phys Mech Astron 2016;59:614601. https://doi.org/10.1007/s11433-015-5712-5.

[10] Morin L, Braham C, Tajdary P, et al. Reconstruction of heterogeneous surface residual-stresses in metallic materials from X-ray diffraction measurements. Mech Mater 2021;158:103882. https://doi.org/10.1016/j.mechmat.2021.103882.

[11] Serrano-Munoz I, Fernández R, Saliwan-Neumann R, et al. Dislocation structures after creep in an Al-3.85%Mg alloy studied using EBSD-KAM technique. Mater Lett 2023;337:133978. https://doi.org/10.1016/j.matlet.2023.133978.

[12] Zhong H, Shi Q, Dan C, et al. Resolving localized geometrically necessary dislocation densities in Al-Mg polycrystal via in situ EBSD. Acta Mater 2024;279:120290. https://doi.org/10.1016/j.actamat.2024.120290.

[13] Li DZ, Zhao XM, Zhang HL, et al. Flow stress-strain curves and dynamic recrystallization behavior of high carbon low alloy steels during hot deformation. J Mater Res Technol 2025;35:3144–60. https://doi.org/10.1016/j.jmrt.2025.02.017.

[14] Mirzaee-Sisan A, Wu G. Residual stress in pipeline girth welds- A review of recent data and modelling. Int J Press Vessels Pip 2019;169:142–52. https://doi.org/10.1016/j.ijpvp.2018.12.004.

[15] Nguyen TN, Wahab MA. The effect of weld geometry and residual stresses on the fatigue of welded joints under combined loading. J Mater Process Technol 1998;77(1-3):201–8. https://doi.org/10.1016/S0924-0136(97)00418-4.

[16] Kainuma S, Mori T. A fatigue strength evaluation method for load-carrying fillet welded cruciform joints. Int J Fatigue 2006;28(8):864–72.

[17] Teng TL, Fung CP, Chang PH. Effect of weld geometry and residual stresses on fatigue in butt-welded joints. Int J Press Vessels Pip 2002;79(7):467–82. https://doi.org/10.1016/S0308-0161(02)00060-1.

[18] Singh PJ, Guha B, Achar DRG. Fatigue tests and estimation of crack initiation and propagation lives in AISI 304L butt-welds with reinforcement intact. Eng Fail Anal 2003;10(4):383–93. https://doi.org/10.1016/S1350-6307(03)00017-7.

[19] Xie X, Jiang W, Luo Y, et al. A model to predict the relaxation of weld residual stress by cyclic load: Experimental and finite element modeling. Int J Fatigue 2017;95:293–301. https://doi.org/10.1016/j.ijfatigue.2016.11.011.

[20] Dehkordi YG, Anaraki AP, Shahani AR. Study of the effective parameters on welding residual stress relaxation in aluminum cylindrical shells under cyclic pressure. ThinWalled Struct 2019;143:106235. https://doi.org/10.1016/j.tws.2019.106235.

[21] Gao J, Cong J, Zhou S, et al. Effect of ultrasonic rolling on crack growth behavior of TC4 titanium alloy laser weld under overload condition. Theor Appl Fract Mech 2025;138:104910.

[22] Li C, Zhao L, Xu L, et al. Insights on microstructure evolution of austenite welded joints subjected to creep-fatigue loading. J Mater Res Technol 2024;30:8635–47. https://doi.org/10.1016/j.jmrt.2024.05.248.